

Active Interaction Force Control for Omnidirectional Aerial Contact-Based Inspection

Karen Bodie*, Maximilian Brunner*, Michael Pantic*, Stefan Walser, Patrick Pfändler, Ueli Angst, Roland Siegwart, and Juan Nieto

Abstract—This paper presents and validates two approaches for active interaction force control and planning for omnidirectional aerial manipulation platforms, with the goal of aerial contact inspection in unstructured environments. We extend upon an axis-selective impedance controller to present a variable axis-selective impedance control which integrates direct force control for intentional interaction, using feedback from an on-board force sensor. The control approaches aim to reject disturbances in free flight, while handling unintentional interaction, and actively controlling desired interaction forces. A fully actuated and omnidirectional tilt-rotor aerial system is used to show capabilities of the control and planning methods. Experiments demonstrate disturbance rejection, push-and-slide interaction, and force controlled interaction in different flight orientations. The system is validated as a tool for non-destructive testing of concrete infrastructure, and statistical results of interaction control performance are presented and discussed.

Index Terms—Aerial Interaction, Force Control, Omnidirectional, MAV, Inspection, Planning.

I. INTRODUCTION

THE DEMAND for industrial contact inspection with aerial robots has been growing rapidly in recent years, coinciding with the development of fully actuated *micro aerial vehicles* (MAVs) for aerial interaction [1]–[5]. A compelling and urgent case exists with aging concrete infrastructure, where a rising amount of required inspection is faced with a lack in capacity to meet the need by traditional means [6]. Early inspection promises a more efficient and intelligent approach to long term maintenance, and a great cost savings when combined with automation. Technologies for *non-destructive testing* (NDT), such as potential mapping, permit detection of corrosion far earlier than visual assessment [7], but require sustained contact between the sensor and structure. While MAVs have been embraced as a solution for efficient visual inspection of infrastructure [8], contact-based inspection still requires extensive human labor and the use of large supporting inspection equipment. Extending the capabilities of MAVs to perform contact inspection is the next obvious step, but also a difficult one: We now require a floating base to carry a sensor payload and to exert precise forces on the

environment in any direction, while at the same time rejecting other sources of disturbance.

With new developments in inspection sensor technology, several small and light-weight devices have emerged which make MAV-based inspection a feasible reality [9], [10]. The task remains to tackle combined interaction force control with disturbance rejection on an autonomous MAV. Recent research in *omnidirectional micro aerial vehicles* (OMAVs)—fully actuated MAVs capable of exerting an arbitrary force and torque—begins to reach this goal. The ability to exert a six *degrees of freedom* (DOF) force and torque allows for decoupling of the system’s translational and rotational dynamics, enabling precise interaction with the environment while maintaining stability. However, making this solution a viable alternative to traditional inspection requires an OMAV with on-board sensing, high force generation in all directions, and accurate and reliable interaction control in six DOF.

Tilt-rotor OMAVs offer omnidirectional flight and high interaction force capabilities [11], but the additional complexity of such a system can increase model uncertainty. In addition, flying systems in general are subject to airflow disturbances (from external sources or propeller down wash), which are difficult to perceive or predict. Accurate control of interaction forces requires separating such disturbances and model error from interaction forces. With recent technological improvements, force sensors have reduced in size and improved in capability, enabling direct sensing of interaction forces on a MAV subject to various other disturbances and uncertainties.

A. Related Literature

Interaction control techniques have been actively explored since the 1970’s for fixed-base manipulators, but have not been possible for aerial robots until the past decade. Aerial interaction with traditional rotor-aligned MAVs has been achieved to varying degrees [12], despite known limitations due to underactuation [5].

OMAVs are now entering the aerial robotics curriculum [13], with the ability to control force and torque in six DOFs without compromising system stability. Platform morphologies can be force-omnidirectional only [5], [14], or capable of full pose omnidirectionality [4], [11]. They can be fully actuated by non-parallel fixedly tilted rotors [4], [5], or with actively tilting rotor groups [1], [15]. Handling of disturbances requires their observation, and has been successfully achieved on flying systems using momentum-based approaches [16], [17]. Several OMAVs have further performed contact inspection tasks of industrial structures [2], [3], but without direct (closed-loop) force control.

Methods for direct force control of fixed-base manipulators are well established [18], [19], typically switching controller

* Authors contributed equally to this work.

K. Bodie, M. Brunner, M. Pantic, S. Walser, R. Siegwart, and J. Nieto are with the Autonomous Systems Lab, ETH Zürich, Zurich, Switzerland [kbodie, mabrunner, mpantic]@ethz.ch.

P. Pfändler and U. Angst are with the Institute for Building Materials, ETH Zürich, Zurich, Switzerland

Manuscript submitted to IEEE T-RO December 29, 2019. © 2020 IEEE. Personal use of this material is permitted. Permission from IEEE must be obtained for all other uses, in any current or future media, including reprinting/republishing this material for advertising or promotional purposes, creating new collective works, for resale or redistribution to servers or lists, or reuse of any copyrighted component of this work in other works.

modes when contact is detected. Switching controllers, however, are particularly unsuitable for flying systems due to the increased difficulty of contact estimation for a floating base in the presence of external disturbances. Recent improvements for force-controlled manipulators such as intelligent collision detection [20] and handling of contact loss during force control [21] are increasing commercial adoption. We can look to state-of-the-art manipulator control techniques as inspiration for the control of newly capable fully actuated flying systems, keeping in mind the fundamental differences of a floating base system.

Spatio-temporal trajectory planning is needed to execute high-level contact inspection tasks and drive the MAV to the surface, in contact and away again. For flight in free space, polynomial trajectories are widely used for underactuated MAVs [22]. Surface-based planning for inspection and interaction has been demonstrated by extracting and connecting viewpoints based on triangulated meshes such that there is one potential view-point per mesh face [23], [24].

B. Contributions and Extensions of Previous Work

In this paper we present the system design of a fully actuated aerial manipulation platform capable of on-board computation, power, and sensing. Two methods for active interaction force control without contact switching are proposed for an OMAV, as well as a planning approach. We elaborate on the contributions shown in our paper presented at RSS 2019 [25]:

- The system design of a novel tilt-rotor OMAV with a rigid manipulator arm.
- A 6 DOF *axis-selective impedance control* (ASIC) for a fully-actuated flying system.
- Experiments showing reliable interaction control, and validation of the system as a tool for contact-based NDT of concrete infrastructure.

We further present the following new contributions:

- Intentional interaction control in the form of direct force control combined with variable ASIC for any omnidirectional aerial system.
- Statistical evaluation and comparison of results.

II. SYSTEM

This chapter describes the OMAV system and hardware, using frame definitions presented in table I and fig. 1.

Symbol	Definition
$\mathcal{F}_* : \{O_*, x_*, y_*, z_*\}$	frame: origin and primary axes
W	inertial (world) frame subscript
B	body-fixed (base) frame subscript
T	tool frame subscript
C	TOF camera frame subscript

TABLE I: Coordinate Frame Definitions

A. System Description

The OMAV used in this work takes the form of a traditional hexarotor with equally spaced arms about the z_B -axis. Each

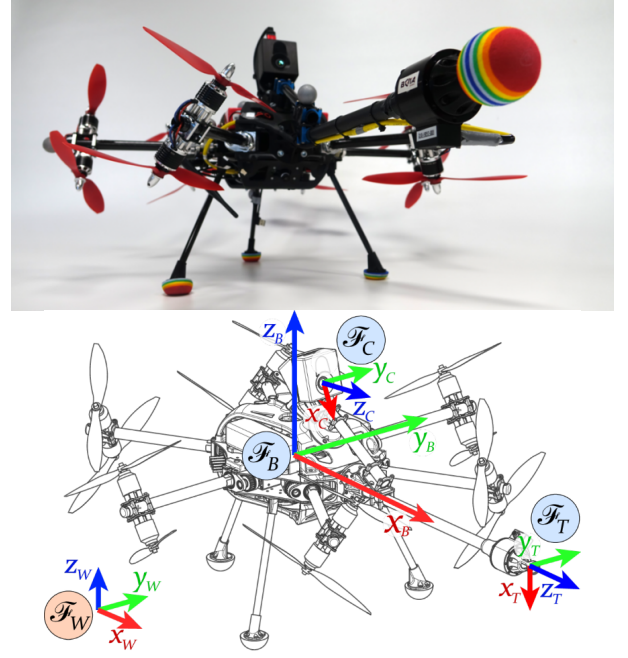


Fig. 1: a) System used for intentional interaction control, equipped with a 6-axis force/torque sensor near the tool tip, and b) world, base, camera and tool coordinate frames.

propeller group is independently tilted by a dedicated servomotor, allowing for various rotor thrust combinations. This tilt action permits high force and torque generation in any direction (allowing omnidirectional hover), while maintaining efficient flight in horizontal hover.

Double rotor groups provide additional thrust for a compact size, with counter-rotating propellers to reduce gyroscopic effects. Symmetrically arranged about the tilt axis, motors also balance rotational inertia and reduce the effort required by the tilt motors.

The platform structure is built from custom carbon fiber, aluminium, and 3D printed plastic parts. Dynamixel XL430 servomotors are used for the tilt arms, and rotors are KDE 885Kv BLDC motors with 9x4.7in propellers. Processing occurs on an on-board Intel NUC i7 computer, and a Pixhawk low level flight controller. Two 6S 3800 mAh Lithium-polymer batteries are mounted for on-board power. The total system mass varies between sensor configurations from 4.75 to 5 kg. Major system parameters are listed in table II.

Parameter	Value	Units
Total system mass	4.75 / 5.0	[kg]
System diameter	0.83	[m]
Rotor group distance to O_b	0.3	[m]
Maximum thrust per rotor group	20	[N]
Number of double rotor groups	6	

TABLE II: Main system parameters

A manipulator arm is rigidly mounted to the platform body, with a tool frame at the tip of the arm. The z_T -axis intersects the body origin, O_B , and lies on the y_B -plane. For the tests in this paper, the z_T -axis is collinear with the x_B -axis. A

Picoflexx Monstar¹ *time of flight* (TOF) camera is rigidly mounted near the base of the arm.

For direct force control tests, the system is equipped with a Rokubi 6-axis force/torque sensor² on the end effector, aligned with the tool frame \mathcal{F}_T . The small size and mass (120g) of the sensor allow integration near the tool tip, which reduces the effect of inertial and aerodynamic disturbances on the sensor measurements. With integrated EtherCAT electronics, no additional processing hardware is required.

B. Parameter Identification

1) *Vehicle center of mass*: The center of mass is subject to change depending on the platform configuration that is used for a specific application. Since it is mostly unfeasible to estimate the *center of mass* (COM) based on the system architecture directly (e.g. a CAD model), we use a calibration procedure to estimate the COM in a calibration flight. During this procedure, the platform performs a trajectory consisting of pitching and rolling while hovering in a constant position. Assuming small angular accelerations, the commanded attitude of the platform in combination with the commanded torque can then be used to compute the position of the COM ${}^B\mathbf{p}_{\text{com}}$ w.r.t. the geometric center.

We record this trajectory over a duration of 30 s and use linear least squares based batch optimization to find ${}^B\mathbf{p}_{\text{com}}$.

2) *Camera and Tool Frame Calibration*: As the TOF camera outputs intensity images on which calibration targets are detectable, we use the kalibr toolbox³ to obtain the transformation from camera optical frame \mathcal{F}_C to the body-fixed frame \mathcal{F}_B .

As the tool frame \mathcal{F}_T changes depending on the mounted tool, its exact location w.r.t. to the body-fixed frame \mathcal{F}_B also needs to be calibrated. If available, an external motion capture system can be used for this. In other cases, we perform a hand-held calibration maneuver where the end-effector is held in steady contact to a flat surface (e.g. floor) and the body is rotated in all three axes about the point of contact. Simultaneously, the current distance and surface normal in camera frame \mathcal{F}_C is calculated from the point cloud of the TOF camera and linear least squares batch optimization is used to obtain the contact point.

III. CONTROL FRAMEWORK

In this section we describe a system model used for control, and introduce two approaches for active interaction control, with the goal of tracking a desired position while simultaneously generating force for interaction. The first approach is a 6 DOF ASIC as a form of indirect force control, as originally described in [25]. The second approach combines direct force and variable ASIC which we will refer to as *intentional interaction control*.

A. Definitions and notation

In the present work, we consider a general rigid-body model for a tilt-rotor aerial vehicle. Refer to table III for definitions of common symbols used throughout the paper. We continue to use the frames presented in table I.

Symbol	Definition
m	mass
\mathbf{J}	inertia tensor
${}^A\mathbf{p}_B$	origin of \mathcal{F}_B expressed in \mathcal{F}_A
\mathbf{R}_{AB}	orientation $\in \text{SO}(3)$ of \mathcal{F}_B expressed in \mathcal{F}_A
${}^A\mathbf{v}_B$	linear velocity of \mathcal{F}_B expressed in \mathcal{F}_A
${}^A\boldsymbol{\omega}_B$	angular velocity of \mathcal{F}_B expressed in \mathcal{F}_A
$\tilde{\mathbf{v}}$	stacked velocity vector $[\mathbf{v} \ \boldsymbol{\omega}]^\top$
\mathbf{F}	force vector
$\boldsymbol{\tau}$	torque vector
$\tilde{\boldsymbol{\tau}}$	wrench vector $[\mathbf{F} \ \boldsymbol{\tau}]^\top \in \mathbb{R}^{6 \times 1}$
$\hat{\tilde{\boldsymbol{\tau}}}$	estimated wrench
$\mathbf{g} = [0 \ 0 \ g \ 0 \ 0 \ 0]^\top$	gravity acceleration vector, $g = -9.81 \text{ m s}^{-2}$

TABLE III: Symbols and definitions

B. Assumptions

To simplify the system model, we assume that the body is rigid, and that body axes correspond with the principal axes of inertia. Thrust and drag torques are assumed proportional to squared rotor speeds, which are instantly achievable without transients. We further assume that tilt motor dynamics are negligible compared to the whole system dynamics, and tilt mechanism backlash and alignment errors are small. Airflow interference between propeller groups is assumed not to effect a significant net wrench on the system.

C. System Model

The simplified system dynamics are derived in the Lagrangian form as

$$\mathbf{M}\dot{\tilde{\mathbf{v}}} + \mathbf{C}\tilde{\mathbf{v}} + \mathbf{g} = \tilde{\boldsymbol{\tau}}_{\text{act}} + \tilde{\boldsymbol{\tau}}_{\text{ext}} \quad (1)$$

where $\mathbf{M} \in \mathbb{R}^{6 \times 6}$ is the symmetric positive definite inertia matrix and $\mathbf{C} \in \mathbb{R}^{6 \times 6}$ contains the centrifugal and Coriolis terms. The terms $\tilde{\boldsymbol{\tau}}_{\text{act}}$ and $\tilde{\boldsymbol{\tau}}_{\text{ext}} \in \mathbb{R}^{6 \times 1}$ are both stacked force and torque vectors exerted on the system respectively by rotor actuation and external sources (e.g. contact or wind disturbances).

Tracking error terms are defined in \mathcal{F}_B in eq. (2). The trajectory is transformed from the inertial frame to compute the error, and we stack the resulting pose and generalized velocity errors.

$$\begin{aligned} \mathbf{e}_p &= \mathbf{R}_{BW}(\mathbf{w}\mathbf{p} - \mathbf{w}\mathbf{p}_{\text{ref}}) \\ \mathbf{e}_R &= \frac{1}{2} (\mathbf{R}_{WB,\text{ref}}^\top \mathbf{R}_{WB} - \mathbf{R}_{WB}^\top \mathbf{R}_{WB,\text{ref}})^\vee \\ \mathbf{e}_v &= {}^B\mathbf{v} - \mathbf{R}_{BW}\mathbf{w}\mathbf{v}_{\text{ref}} \\ \mathbf{e}_\omega &= {}^B\boldsymbol{\omega}_{WB} - \mathbf{R}_{BW}\mathbf{w}\boldsymbol{\omega}_{WB,\text{ref}} \end{aligned} \quad (2)$$

$$\begin{aligned} \tilde{\mathbf{e}}_p &= [\mathbf{e}_p^\top \ \mathbf{e}_R^\top]^\top \in \mathbb{R}^{6 \times 1} \\ \tilde{\mathbf{e}}_v &= [\mathbf{e}_v^\top \ \mathbf{e}_\omega^\top]^\top \in \mathbb{R}^{6 \times 1} \end{aligned} \quad (3)$$

¹<https://pmdtec.com/picofamily/monstar/>

²<https://www.botasys.com/rokubi>

³<https://github.com/ethz-asl/kalibr>

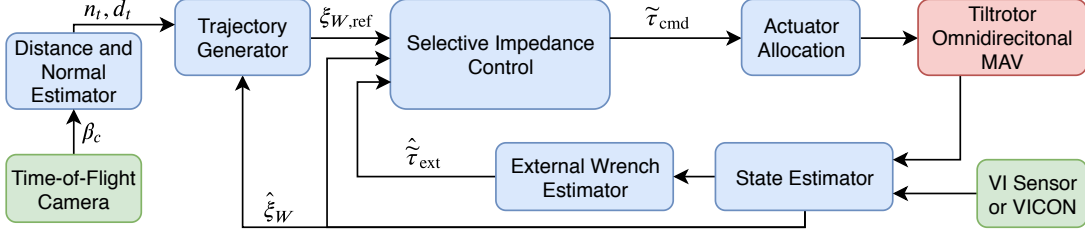


Fig. 2: Block diagram of the ASIC framework, with system state, $\xi = \{p, v, \dot{v}, R, \omega, \dot{\omega}\}$. Surface normal, n_t , and distance, d_t , are extracted from point cloud β_c provided by the TOF camera. Sensors are in green and the physical system in red.

D. External Wrench Estimation

In order to account for the influence of contact forces, we employ an external wrench estimator using a generalized momentum approach. Our implementation follows the method described in [26], and is expressed as

$$\dot{\hat{\tau}}_{\text{ext}} = K_I \left(M\tilde{v} - \int \left(\tilde{\tau}_{\text{cmd}} - C\tilde{v} - g + \hat{\tau}_{\text{ext}} \right) dt \right), \quad (4)$$

where we assume that the commanded $\tilde{\tau}_{\text{cmd}}$ is able to achieve the desired actuation wrench $\tilde{\tau}_{\text{act}}$. The positive definite diagonal observer matrix $K_I \in \mathbb{R}^{6 \times 6}$ acts as an estimator gain. Differentiating (4), a first-order low-pass filtered estimate $\hat{\tau}_{\text{ext}}$ of the external wrench τ_{ext} is obtained:

$$\dot{\hat{\tau}}_{\text{ext}} = K_I (\tilde{\tau}_{\text{ext}} - \hat{\tau}_{\text{ext}}) \quad (5)$$

Note that (4) allows estimation of external forces and torques without the use of acceleration measurements, only requiring linear and angular velocity estimates.

E. Control Approach 1: Axis-Selective Impedance Control

The first approach aims to control the mechanical impedance of the system, with the environment treated as an admittance [27]. This controller indirectly regulates a wrench exerted by the system on its environment for safe and stable interaction. The same controller can account for interaction and free flight without switching, by tracking a trajectory into a state of collision. We can take advantage of the system's full actuation to implement an impedance controller with apparent inertia that can be individually selected on each axis in 6 DOF, to reject disturbances in some directions while exhibiting compliant behavior in others.

Our implementation is based on the method described in [28], a block diagram of the framework is shown in fig. 2. We take the simplified dynamics of the system from (1) and choose the desired closed loop dynamics of the system to be

$$M_v \dot{\tilde{v}} + D_v \tilde{v} + K_v \tilde{e}_p = \tilde{\tau}_{\text{ext}}, \quad (6)$$

where M_v , D_v , and $K_v \in \mathbb{R}^{6 \times 6}$ are positive definite matrices representing the desired apparent inertia, desired damping, and desired stiffness of the system. We can then derive the applied control wrench by substituting $\dot{\tilde{v}}$ from (6) into (1) as follows:

$$\tilde{\tau}_{\text{cmd}} = (MM_v^{-1} - \mathbb{I}_6) \hat{\tau}_{\text{ext}} - MM_v^{-1} (D_v \tilde{e}_v + K_v \tilde{e}_p) + C\tilde{v} + g \quad (7)$$

Since the stiffness and damping properties of interaction depend highly on the apparent inertia, we first normalize these matrices with respect to the true system inertia as $\overline{M}_v = M^{-1}M_v$, then express stiffness and damping as $\overline{D}_v = \overline{M}_v^{-1}D_v$ and $\overline{K}_v = \overline{M}_v^{-1}K_v$. In addition, the selective impedance can be rotated into a desired frame, in this case the fixed end-effector frame, using $R = \text{blockdiag}\{R_{BT}, R_{BT}\}$, where R_{BT} is a rotation matrix expressing the orientation of the tool frame in the body-fixed frame. We then rewrite (7) as

$$\tilde{\tau}_{\text{cmd}} = (R^T \overline{M}_v^{-1} R - \mathbb{I}_6) \hat{\tau}_{\text{ext}} - \overline{D}_v \tilde{e}_v - \overline{K}_v \tilde{e}_p + C\tilde{v} + g. \quad (8)$$

Integration of a rigidly attached end-effector to the system simplifies the problem of selective stiffness in impedance control. The apparent mass is set to a low value along the z_T -axis, less than the system mass to exhibit compliant behavior. Orienting the z_T -axis normal to the desired contact surface is then sufficient to ensure compliance in the contact direction and stiff behavior in the orthogonal plane, and a stiff response to error in orientation.

F. Control Approach 2: Intentional Interaction Control

By the same mechanism that the wrench estimation reduces model error and rejects aerodynamic disturbances, it suffers as a measurement for interaction control. The momentum-based external wrench contains an accumulation of force and torque unrelated to the point of interaction, and in many cases cannot be used for direct force tracking. The concept presented here takes advantage of a multi-axis force sensor mounted at the tool tip to resolve differences in interaction forces and other aerial disturbances.

This control approach which we'll refer to as *intentional interaction control* embodies the higher level idea of purposeful interaction, and should be used with a planner that is aware of its environment and the interaction task. Force control is only attempted when it is explicitly communicated by the planner, and tracking of the pose trajectory for all axes is performed at all times. At points of interaction, the desired tool trajectory traces the surface exactly, and an additional vector provides a desired force command. When free flight is intended, this interaction force component is zero.

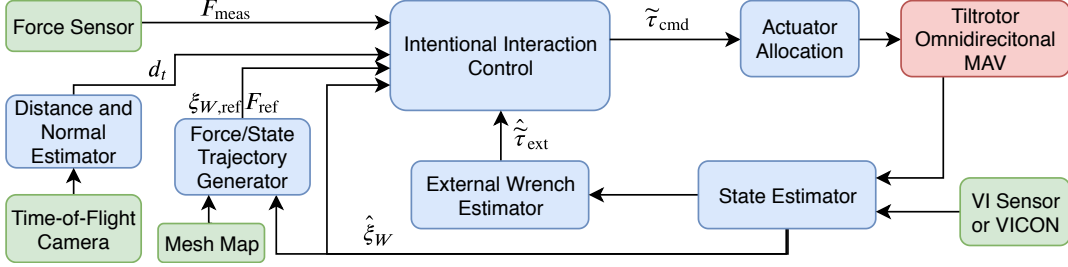


Fig. 3: Block diagram of the intentional interaction control framework, combining direct force control with variable ASIC. The primary difference from fig. 2 is the integration of direct force F_{meas} and distance d_t sensing in the controller.

1) *Variable Axis-Selective Impedance Control*: One weakness of the first control approach is that when a low apparent mass is set along the axis of the end effector, this axis is also compliant to airflow disturbances and model error.

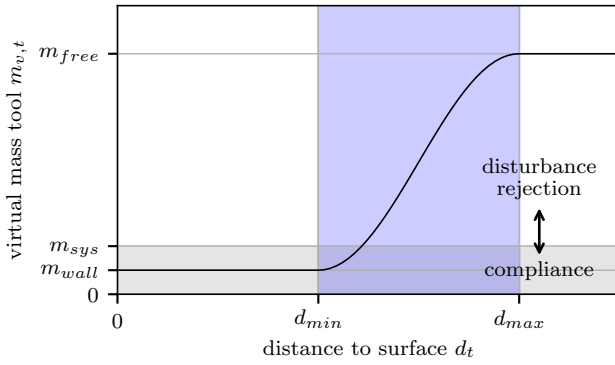


Fig. 4: Variable impedance in the z_T direction as a function of wall distance d_t , with transition zone shown in blue.

We address this case by using the distance measurement d_t of a surface from the tool frame along z_T , as described in section IV-A. In free flight, when surfaces are far away, the virtual mass $m_{v,\text{free}}$ along the end effector axis is as high as all other axes to reject disturbances. Within a range from d_{max} to d_{min} from the surface, that value ramps down to $m_{v,\text{wall}}$ according to a sine function to exhibit compliance (fig. 4). The resulting apparent mass is calculated as follows:

$$c_{v,T} = \begin{cases} 1, & \text{if } d_t \leq d_{\min} \\ 0.5(1 + \cos(\frac{d_t - d_{\min}}{d_{\max} - d_{\min}}\pi)), & \text{if } d_{\min} < d_t \leq d_{\max} \\ 0, & \text{otherwise} \end{cases} \quad (9)$$

$$m_{v,T} = c_{v,T}(m_{v,\text{free}} - m_{v,\text{wall}}) + m_{v,\text{wall}}$$

$$\mathbf{M}_v = \text{diag}\{[m_{v,\text{free}} \quad m_{v,\text{free}} \quad m_{v,T} \quad J_v \quad J_v \quad J_v]^\top\} \quad (10)$$

Note that the apparent inertia J_v is equal in all axes in order to reject torque disturbances and to track the desired attitude while in contact.

2) *Direct force control*: We aim to apply direct force control in order to exert a specific force onto a surface. The

reference force is given by a trajectory $F_{\text{ref}}(t)$ that is defined according to the task. A force trajectory is only acted upon when there is confidence that the reference force can exist at a location near enough to the target. This confidence is a function of the perceived surface distance d_t and the tool position error e_t in the direction of desired force (eq. (12)), as calculated in eq. (15). The value is smoothly transitioned with a first-order filter with coefficient c_λ to avoid step inputs at the start or end of a non-zero desired force. We arrive at the computation of the confidence factor λ_k which represents λ at time step k .

$$e_t = \mathbf{p}_t - \mathbf{p}_{t,\text{ref}} \in \mathbb{R}^{3 \times 1} \quad (11)$$

$$e_{t,F_{\text{ref}}} = \frac{e_t \cdot \mathbf{F}_{\text{ref}}}{\|\mathbf{F}_{\text{ref}}\|} \quad (12)$$

$$\lambda_d = \begin{cases} 1, & \text{if } d_t \leq d_{\min} \\ 0.5(1 + \cos(\frac{d_t - d_{\min}}{d_{\max} - d_{\min}}\pi)), & \text{if } d_{\min} < d_t \leq d_{\max} \\ 0, & \text{otherwise} \end{cases} \quad (13)$$

$$\lambda_e = \begin{cases} 1, & \text{if } e_{t,F_{\text{ref}}} \leq e_{\min} \\ 0.5(1 + \cos(\frac{e_{t,F_{\text{ref}}} - e_{\min}}{e_{\max} - e_{\min}}\pi)), & \text{if } e_{\min} < e_{t,F_{\text{ref}}} \leq e_{\max} \\ 0, & \text{otherwise} \end{cases} \quad (14)$$

$$\lambda_k = \begin{cases} c_\lambda \lambda_d \lambda_e + (1 - c_\lambda) \lambda_{k-1}, & \text{if } \|\mathbf{F}_{\text{ref}}\| > 0 \\ 0, & \text{otherwise} \end{cases} \quad (15)$$

The behavior of the combined force and impedance control is shown in fig. 5. In the nominal case, the planner commands a path in free flight which the controller is able to achieve, and a desired force is commanded only when the sensed distance d_t and projected tool error $e_{t,F_{\text{ref}}}$ are small. In the case where the set point is behind the wall, the controller uses compliant impedance control in the direction of the end effector to perform its task as well as possible. When a force is then commanded, λ is 1 and force control is fully active. When the set point is in front of the wall between d_{\min} and d_{\max} , there is a transition phase where λ is between 1 and 0, a compromise between trying to achieve force control and maintain trajectory tracking. In the case where the wall is not sensed within d_{\max} , λ is 0 and no force control is attempted.

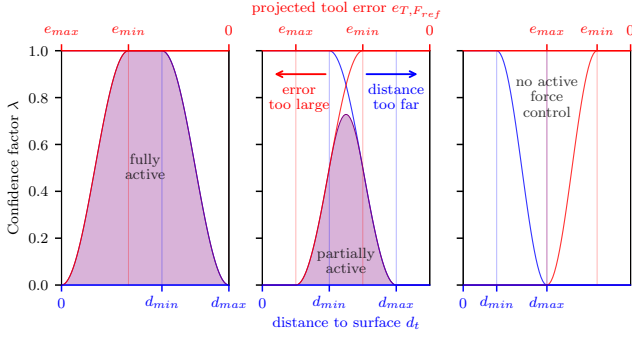


Fig. 5: Confidence factor λ as a function of wall distance d_t , and projected tool error $e_{T,F_{ref}}$. The solid area indicates the proportion of force control used.

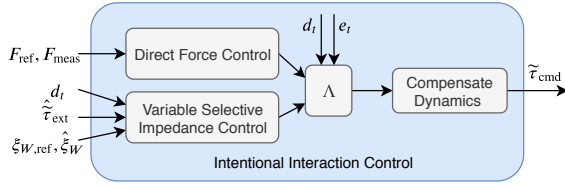


Fig. 6: Diagram of intentional interaction control, with impedance control varying apparent mass along the tool axis as a function of the sensed distance d_t . Direct force control is added selectively as a function of d_t and the tool error e_t .

3) *Unified wrench command*: The selection matrix, Λ , orients the confidence factor λ from eq. (15) in the direction of desired force F_{ref} using the rotation $R_{F_{ref}z}$, and is constructed as follows:

$$\Lambda = R_{F_{ref}z} \begin{bmatrix} 0 & 0 & 0 \\ 0 & 0 & 0 \\ 0 & 0 & \lambda \end{bmatrix}, \quad R_{F_{ref}z}^T \in \mathbb{R}^{3 \times 3} \quad (16)$$

$$\tilde{\Lambda} = \text{blockdiag}\{\Lambda, \mathbf{0}_{3,3}\} \in \mathbb{R}^{6 \times 6} \quad (17)$$

We augment this matrix to 6 DOF with zeros since we have a point end effector, but this could be extended for intentional interaction torques. The matrix positively selects direct force control commands. We use a *proportional-integral* (PI) control scheme with a feed forward force term to track the given reference force based on the force tracking error e_f and the reference force $F_{ref,B}$. We assume that the interaction force F_t at the end effector can be measured by an on-board sensor.

$$e_f = F_t - F_{ref} \quad (18)$$

$$F_{dir} = \frac{1}{m} \Lambda \left(-F_{ref,B} + K_{f,p} e_f + K_{f,i} \int e_f dt \right) \quad (19)$$

$$\tilde{\tau}_{dir} = [F_{dir}^T \quad 0 \quad 0 \quad 0]^T \in \mathbb{R}^{6 \times 1} \quad (20)$$

Using M_v from eq. (10) and normalizing by the system mass as before, we compute the impedance control command

$$\tilde{\tau}_{imp} = (\mathbb{I}_6 - \tilde{\Lambda})(R^T \bar{M}_v^{-1} R - \mathbb{I}_6) \hat{\tau}_{ext} - \bar{D}_v \tilde{e}_v - \bar{K}_v \tilde{e}_p, \quad (21)$$

where the selection matrix counterpart $(\mathbb{I}_6 - \tilde{\Lambda})$ is used to remove the component of the momentum-based wrench estimate in the direction of desired interaction.

The two control commands are then combined and compensated for nonlinear dynamic effects and gravity. Since the system COM is not located at the geometric center of control, we use a feed forward term to compensate for the torque caused by the offset. The final resulting wrench command is shown in eq. (24), and shown as a block diagram in fig. 6.

$$\tilde{\tau}_{cmd}^* = \tilde{\tau}_{dir} + \tilde{\tau}_{imp} + C\tilde{v} + g \quad (22)$$

$$\tilde{\tau}_{com} = \begin{bmatrix} \mathbf{0}_{3,1} \\ {}_B p_{com} \times \tau_{cmd} \end{bmatrix} \quad (23)$$

$$\tilde{\tau}_{cmd} = \tilde{\tau}_{cmd}^* + \tilde{\tau}_{com} \quad (24)$$

G. Force Sensor Filtering

Any additional mass on the end of the force sensor will lead to inertial forces and torques from dynamic movement. This can be modeled with known pose of the end effector and static and dynamic parameter identification, but in our case is ignored due to very low mass. We still expect to see noise from vibration, which can be addressed with a filter.

We use a 2nd-order low pass butterworth filter with a cutoff frequency of 5 Hz. This filter yields smooth force measurements with reasonable latency for surface inspection tasks.

IV. DISTANCE ESTIMATION AND PLANNING FOR INTERACTION

A. Surface Distance Estimation

For surface distance estimation the predicted contact point is defined as the intersection of an observed surface and the z_t -axis (C_t^0 in fig. 7). In order to estimate the distance to this point, a point cloud is obtained from the TOF camera and all points within a certain distance to the z_t -axis are selected. This subset of 3D points is subsequently called A_t^0 . The 3D contact point location is obtained by an unweighted average of all points in A_t^0 .

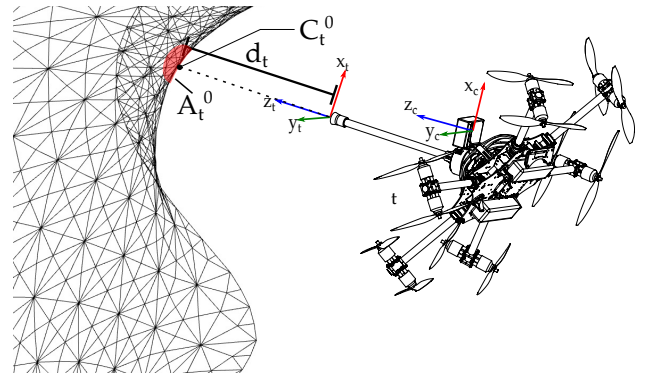


Fig. 7: Distance and normal estimation: C_t^0 is the contact point defined by the intersection of the z_t -axis and the observed surface. d_t depicts the distance to the contact point, and A_t^0 is the set of 3D points used to estimate normal and distance.

For the experiments in this work the radius of A_t^0 is chosen to be 0.1 m, which yields approximately 2600 points for distance and normal estimation when in contact and about 500 at a distance of $d_t = 1$ m. By averaging this large amount of individual measurements per estimate, we obtain a smooth, exact and very low noise distance measurement.

B. Force Trajectory Planning

Interacting with a surface requires knowledge about the location and orientation of the surface. We use the TOF camera to obtain a point cloud of the surface to interact with, which is then converted to a triangular mesh with face and vertex normals by using Poisson surface reconstruction [29].

A polynomial trajectory consisting of the desired setpoints for position, orientation, linear- and angular velocity and acceleration as well as desired tool force is then planned. The trajectory drives the tool to the contact point on the surface and aligns the z_T axis with the surface normal obtained from the mesh reconstruction. The contact force trajectory is planned by holding the position and orientation at the desired contact location while ramping up the force along z_T to the desired magnitude using a sinusoidal ramp.

V. EXPERIMENTS

Through a series of experiments we demonstrate the capabilities and applications of the system.

- V-A: System response to an external disturbance with (variable) ASIC.
- V-B: Repeatable push-and-slide tracking on a planar surface, while rejecting disturbances due to surface friction.
- V-C: Direct force control in interaction.
- V-D: Robustness to planner error, when a desired force is given in free space or within an obstacle.
- V-E: Viability as an infrastructure contact testing tool.
- V-F: Statistical evaluation of the intentional interaction force control contacting an undulating structure.

State estimation for the experiments in this paper is carried out by fusing on-board *inertial measurement unit* (IMU) data with external motion capture information from a VICON system. Experiments with fully on-board state estimation are documented in our previous paper [25]. A video showcasing the experiments can be accessed at youtu.be/7NvIk11xo-c.

A. Rope Pull Disturbance in Free Flight

In this section, we first present an experiment consisting of three tests that validate the effectiveness of ASIC. In a second experiment we show the advantage of *variable* ASIC.

1) *Axis-Selective Impedance Control*: In this experiment, we evaluate the behaviour of the system with different selective apparent inertia values, demonstrating the ability to reject large disturbances in certain directions. The system is commanded to hold a reference pose 1 m above the ground in free flight. A cord is tied to the tool tip of the rigid manipulator arm, which is aligned with the x_B -axis. The other end of the cord is pulled manually to generate an external wrench. The experimental parameters are listed in table IV, where m_x^* , m_y^* ,

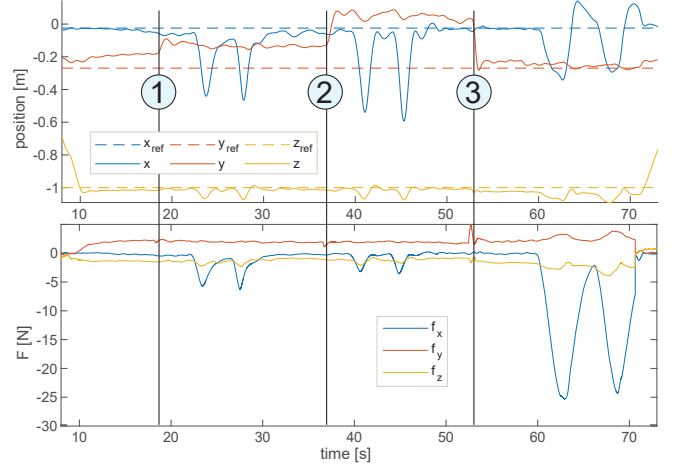


Fig. 8: Pose tracking and wrench estimation for rope pulling at the tool tip along the z_T -axis in free flight.

Experiment	Controller	m_x^*	m_y^*	m_z^*	J_v^*
Rope pull 1	ASIC	0.25	0.25	1.0	1.0
Rope pull 2	ASIC	0.1	0.1	1.0	1.0
Rope pull 3	ASIC	5.0	5.0	1.0	1.0
Push and slide	ASIC	0.25	5.0	5.0	5.0

Experiment	Controller	m_{wall}^*	m_{free}^*	J_v^*
Rope pull	Variable ASIC	0.5	5.0	5.0
Wall push	Variable ASIC	0.5	5.0	5.0
Concrete NDT	Intentional Interaction	0.5	5.0	5.0
Und. surface	Intentional Interaction	0.5	5.0	5.0

TABLE IV: Controller parameters for experiments

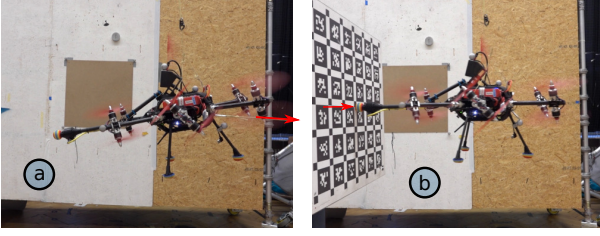
*Inertial parameters are multipliers of the system inertia.

and m_z^* are the relative apparent masses along the body axes, and J_v^* is the relative virtual inertia on all axes. Test results are shown in fig. 8, where two pulls of the rope are made for each set of apparent inertia parameters, approximately along the negative x_B -axis.

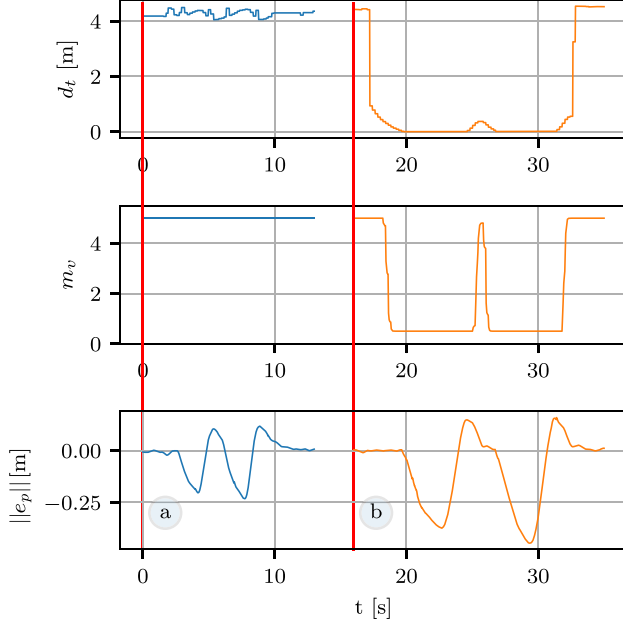
Tests 1 and 2 show similar results: a compliant response to a disturbance force in the direction of pull. Apparent mass values in x_B and y_B are lower than the actual system mass, meaning that force disturbances in these directions will be tracked in the controller, while the *proportional-derivative* (PD) component simultaneously tracks the reference trajectory. Results in test 2 show a larger movement in response to a smaller applied force in low impedance directions, relative to test 1. The remaining degrees of freedom have high apparent inertia values, actively rejecting detected disturbances to track the reference trajectory. In test 3, apparent mass in x_B and y_B are set to 5 times the system mass and inertia. Results show positional movement of less than 0.3 m under a lateral disturbance force of 25 N, demonstrating an ability to actively reject large force disturbances. These results motivate impedance parameters chosen for the remaining experiments.

2) *Variable Axis-Selective Impedance Control*: We performed an experiment consisting of 2 trials to show the advantages of variable ASIC. In a first trial (a) we manually pull on a tether that is fixed to the OMAV while hovering at a constant position reference. In a second trial (b) we use

a 1x1m sized plate to push onto the platform's end effector while in hover. Fig. 9b shows the perceived distance d_T , the apparent mass $m_{v,T}$, and the position error e_B in the direction of the end effector during the two trials. The pulling force on the rope in a) represents an unobservable disturbance which is rejected by keeping a high value in m_v . In b), as the distance to the plate's surface is perceived to decrease to zero, the OMAV becomes compliant and decreases the apparent mass, allowing for a larger deviation from the position reference.



(a) Pulling on a cord (left) and pushing with a plate (right). The direction of the disturbance force is indicated by the red arrow.



(b) Perceived tool distance d_t , apparent mass m_v , and position error $\|e_p\|$.

Fig. 9: Comparison of rejecting and compliant behavior.

B. Push-and-Slide Along a Flat Surface with ASIC

We evaluate the system's ability to maintain and reject disturbances from friction, while accurately and repeatably drawing on a whiteboard positioned in a known location. The trajectory traces a spline with the tool point 10 cm behind the surface of the whiteboard. The end-effector is a whiteboard marker with no additional compliance. For compliance the apparent mass is chosen high in all directions, except for the z_T -axis.

Tracking results for position and orientation in the top two plots of fig. 10 show ground truth measurements from the

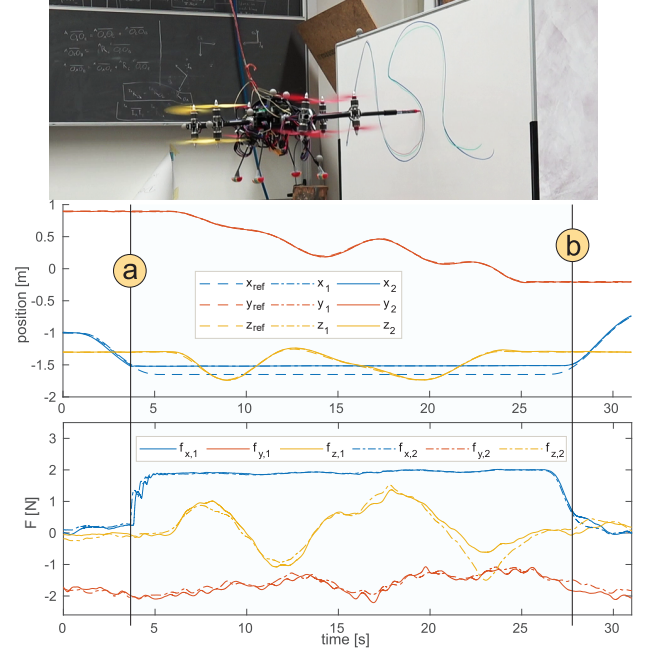


Fig. 10: Pose tracking and wrench estimation for push-and-slide experiments. A shape is drawn on a whiteboard aligned with the x -plane in two separate trials (subscripts 1 and 2) with Vicon state estimation. At time (a), the system contacts the wall, and at (b), resumes free flight.

motion capture system of two trials drawing the same shape on a whiteboard, compared to the reference. In the time interval between (a) and (b), the tool is in contact with the whiteboard, maintaining a consistent force while completing a trajectory.

Without any change in the controller, the system is able to handle transitions in and out of contact with good stability, and without significant tracking error on the surface plane. The system demonstrates rejection of torque and lateral force disturbances caused by surface friction while maintaining a consistent contact force against the wall, as shown in the lower plot of fig. 10.

Offsets in y_B -force and y_B - and z_B -torque in free flight—as well as a small bias in the attitude tracking of the system—are the result of an unaccounted-for offset of the system's center of mass. This result demonstrates that the proposed impedance control can compensate well for model errors, maintaining attitude error within 0.07 rad.

C. Direct Force Tracking Accuracy

In order to evaluate the accuracy of force tracking with *intentional interaction control*, we design a trajectory containing both a pose and a force reference. The position reference is set approximately on the surface of a rigid vertical wall, and the attitude reference sets the z_T -axis orthogonal to the surface plane. The force trajectory changes between 5 N, 10 N, and 20 N. Fig. 11 shows the tracking performance of the force controller. The reference force is tracked consistently, even through fast changes of the set point. The momentum based force estimate adapts more slowly to the change of force but converges to similar values.

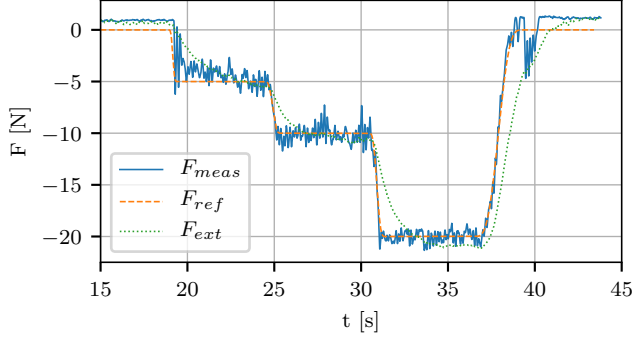


Fig. 11: Tracking of 3 different force references. Dashed lines are the force references in the world frame, solid lines are measured forces at the end effector. The dotted line shows the momentum based force estimate.

We found that both the feed forward term and the integral gain are the most essential parts of the force controller. Increasing the proportional gain usually leads to higher frequency changes in the resulting contact forces, while not significantly improving the response time to reference changes.

Additionally, we test the robustness of the proposed *intentional interaction control* by performing a surface inspection task with multiple contacts with reference forces of 5 N. In a first experiment, we set the position reference slightly in front of the true surface position, and in a second trial we set it slightly behind the true position. Fig. 12 and fig. 13 illustrate that for each trial, the measured force settles at the reference force after a short response time. The experiments show that the direct force control command τ_{dir} compensates the impedance control command τ_{imp} in order to achieve the desired contact force.

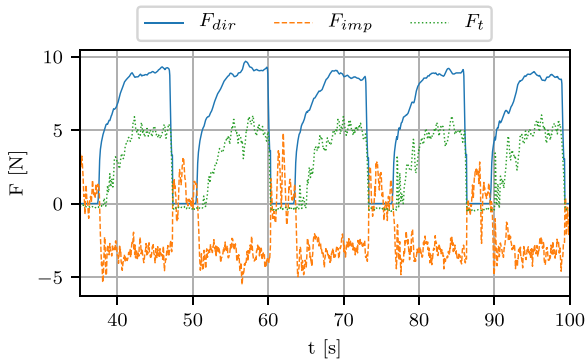


Fig. 12: Direct force control, impedance control, and measured force during contact inspection. Position reference is slightly in front of the wall. Direct force control component compensates for position tracking of impedance control component, tracking the reference force of 5 N.

D. Force Tracking Robustness to Planner Error

To evaluate the robustness of *intentional interaction control* from section III-F to planner error, we specify a desired force

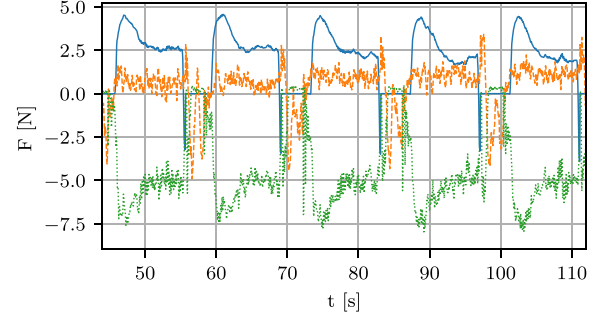


Fig. 13: Contact inspection with position reference behind the wall. Impedance and direct force control components complement to track the reference of 5 N.

in three situations that are not at a contact surface:

- (a) Close to a surface
- (b) 0.25 m in front of the surface
- (c) 0.5 m away from the surface

Fig. 14 shows the resulting behavior for the three scenarios. In a), the platform is close enough to the wall to enable direct force control by increasing the confidence factor λ to 1. In b), the perceived tool distance d_t in combination with the tool error e_B leads to a short increase in λ before being pulled back by the resetting force of the impedance controller. In c), the tool distance d_t is larger than the maximum selected tool distance d_{max} and direct force control is therefore not enabled. In all cases, the system responds to planner error in a stable way, and is able to continue executing a compromise of the combined state and force trajectory.

E. Potential Field Concrete Inspection Task

Similar to experiments in [25], we conduct an autonomous contact inspection task on a sample of reinforced concrete.

We equip the end effector with an NDT contact sensor that measures both the electrical potential difference between a saturated Copper Sulfate Electrode (CSE) and the embedded steel, and the electrical resistance between the sensor on the concrete surface and the steel reinforcement. Electrical potential and resistance results can be used as an indicator for the corrosion state of the steel [30]. A cable is connected to the reinforcement in the concrete structure, and is physically routed to the sensor on the flying system to perform the measurements. The concrete specimen used for this experiment has a known corrosion spot at a certain location and a constant cover depth. The corrosion state can therefore be evaluated against this information. The concrete block is positioned at a known location, and a trajectory is defined to contact 9 points at 5 cm intervals along the surface. Each point is held for a duration of 10 s, during which a reference force of 5 N is requested.

Fig. 15 compares the autonomously measured potentials of two flights with manually measured potentials along the sample, measured before and after the flights. The plot shows that the controller is able to hold contact between the end effector and the sample to allow accurate measurements of the potential.

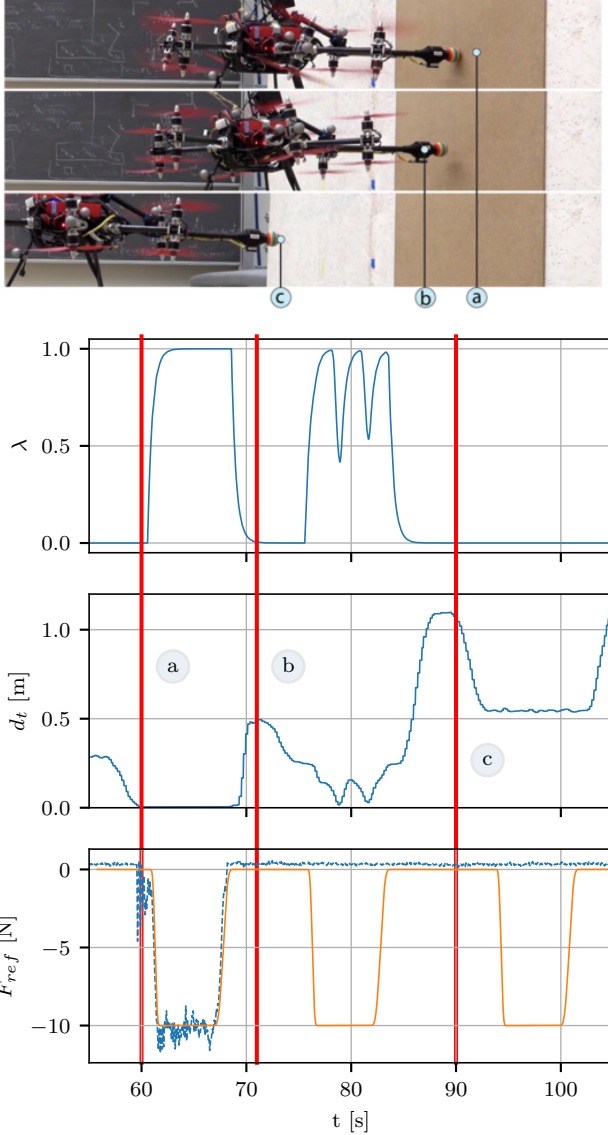


Fig. 14: Confidence factor λ , wall distance and force reference show behavior for a set point a) behind the wall, b) in front of the wall by 0.25m, and c) >0.5 m away from the wall.

F. Statistical Validation on an undulating Surface

We perform a statistical evaluation of the *intentional interaction control* to validate its robustness and performance. The repeated random experiments aim to characterize the system in a more diverse, less controlled environment in order to show its applicability to complex tasks.

As a test surface, we use a doubly curved wooden surface with a size of approx. $1\text{ m} \times 1.8\text{ m}$, which is mapped and used for planning as described in section IV-B. Fig. 16 visualizes the randomly selected 42 contact locations at which we command the OMAV to exert a force of 10 N perpendicular to the surface for 5 s.

Figure 17 overlays the force along the z_T axis for all trials with the time aligned beginning from the first force command. In all 42 trials the system was able to hold contact and keep position and orientation regardless of the local surface

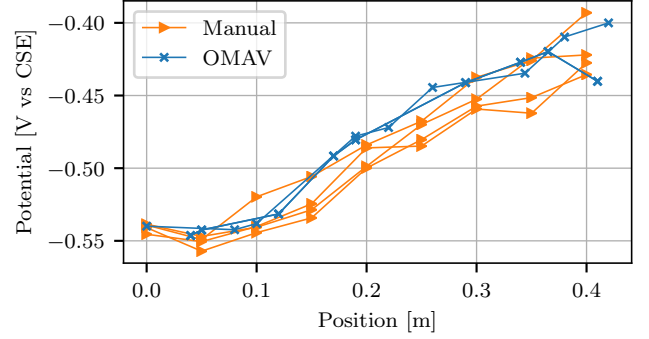
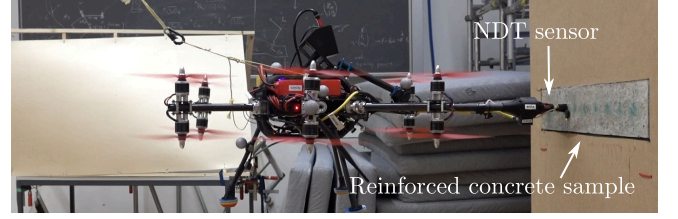


Fig. 15: Potential field concrete inspection experiment. Top: System in contact with one of 9 sampling points. Bottom: Comparison of potential mapping results for measurements taken during two autonomous flights (OMAV), and four manual measurements along a reinforced concrete block sample.

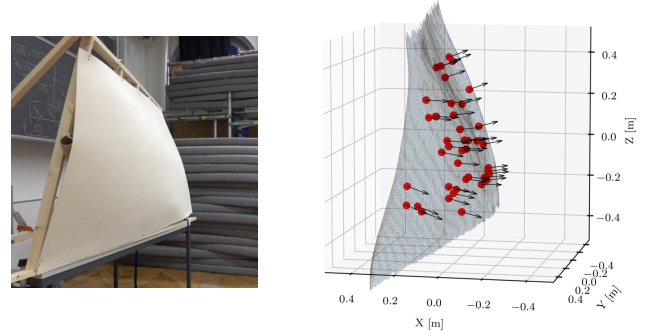


Fig. 16: Undulating wooden wall used for experiments (left), randomly sampled contact locations (red dots) and their surface normal (black arrows).

geometry. The desired force of 10 N could be achieved in almost all trials. However, the stabilization time of the force magnitude is dependant on the local springiness of the surface. In extreme cases, such as trial 38, the surface deflected by multiple centimeters as visualized in figure 17.

An important application-driven evaluation is the 2d tool position error on the surface, which combines the effect of the body position and attitude error. Figure 18 visualizes the statistics of the tool position error for each individual trial as violin plots. The trials are sorted by their pitch reference angle, where negative pitch indicates a downward pitch of the OMAV.

Note that the tool position does not change after contact is made steadily, thus the plot in figure 18 uses data obtained whenever the tool is closer than 5 cm to the surface.

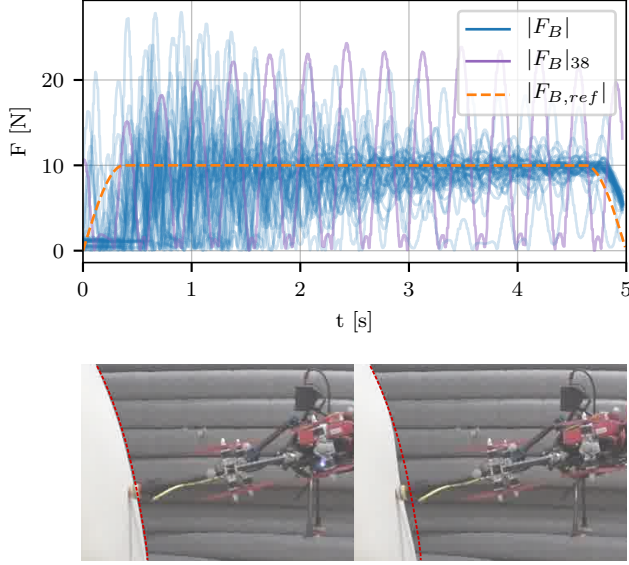


Fig. 17: Top: Overlay of interaction force magnitude during 42 individual trials. Time $t = 0$ corresponds to the first force command issued. Trial 38 is marked separately, as the force did not stabilize. Bottom: Frames 0.15 s apart during Trial 38. Deformation of the surface is clearly visible. The red dotted line indicates the nominal surface.

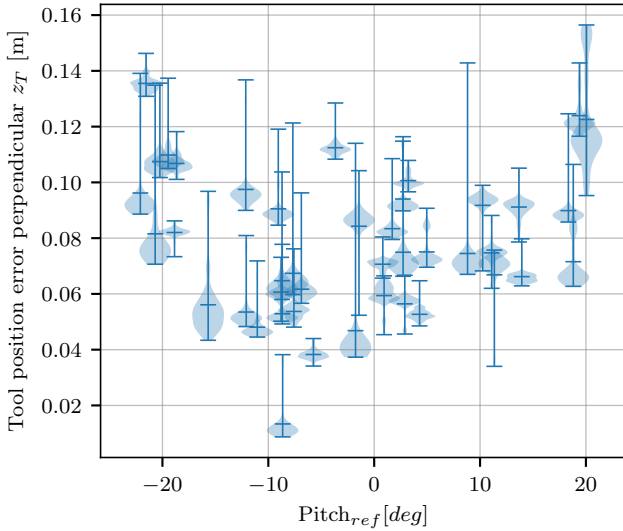


Fig. 18: Tool position error perpendicular to the z_T -axis for each individual trial. Presented data is for each trial whenever the tool is within 5 cm of the surface. Data is truncated such that each trial includes 1250 measurements, about 5 s of data.

Similarly, figure 19 shows the force error along z_T for each individual trial. The two curves at around -17 and -22 degrees pitch that show large densities close to the extreme values correspond to the before discussed cases where the surface springiness leads to force oscillation.

Both the position and force error statistics indicate a slight influence of the pitch reference on the errors. The system

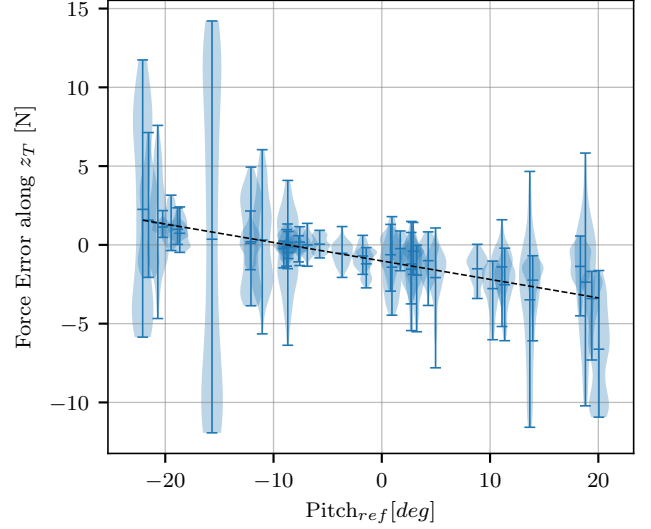


Fig. 19: Force control error vs. desired pitch for each individual trial. Force data is truncated to the last 2.5 s of the interaction duration, allowing the system to stabilize first. The black dotted curve is a linear fit to the mean force error.

slightly overshoots the desired force if it pitches downwards and vice-versa. Overall, the system showed predictable and robust force trajectory executing during all trials.

VI. DISCUSSION

The experiments showed that selective impedance control presents a suitable method for contact inspection, if the axis of desired pressure on the surface is known. Using low apparent mass along this axis allows compliance, while high apparent mass along the axes parallel to the surface yield accuracy in lateral positioning.

If specific interaction forces are required and if the location of the surface is only known with a precision of a few centimeters, variable ASIC in combination with direct force control proved to give good force tracking accuracy. For position references behind or in front of the actual surface, the reference force was achieved in most experiments after few seconds of contact. The use of the confidence factor λ allows simple and smooth transitioning between different stages of flight, which yielded stable and controlled maneuvers while switching from free flight to interaction control.

Regardless of the control, the system's flight performance is considerably sensitive to its hardware calibration. Small changes of the COM or slightly incorrect zeroing of tilt arms can lead to different behavior and might require new calibration. This model error is amplified by unmodeled effects, such as airflow interference or backlash in gears that are driving the tilt arms. We aim to mitigate calibration errors in the future with automatic on-line calibration of relevant physical system properties, such as COM, inertia and tool mass.

Finally, the experiments confirm that the presented control approach combining distance sensing and surface-based force

trajectory planning complete the basis for high-level force interaction tasks to be carried out by OMAVs.

VII. CONCLUSION

In this paper, we presented two approaches for active force control of an omnidirectional micro aerial vehicle. By using additional sensing such as force/torque and surface distance measurements, our system is able to reliably and safely perform force control in a variety of environments.

Extensive experiments demonstrated the feasibility of the proposed system for applications such as non-destructive testing of infrastructure and other contact-based application.

ACKNOWLEDGMENT

This work was supported by funding from ETH Research Grants, the National Center of Competence in Research on Digital Fabrication, and Armasuisse Science and Technology.

REFERENCES

- [1] M. Kamel, S. Verling, O. Elkhatib, C. Sprecher, P. Wulkop, Z. Taylor, R. Siegwart, and I. Gilitschenski, "The Voliro Omnidirectional Hexacopter: An Agile and Maneuverable Tilttable-Rotor Aerial Vehicle," *IEEE Robotics & Automation Magazine*, vol. 25, no. 4, pp. 34–44, 2018.
- [2] A. Ollero, G. Heredia, A. Franchi, G. Antonelli, K. Kondak, A. Sanfeliu, A. Viguria, J. R. Martinez-De Dios, F. Pierri, J. Cortés *et al.*, "The AEROARMS Project: Aerial Robots with Advanced Manipulation Capabilities for Inspection and Maintenance," *IEEE Robotics and Automation Magazine*, 2018.
- [3] M. Tognon, H. A. T. Chávez, E. Gasparin, Q. Sablé, D. Bicego, A. Mallet, M. Lany, G. Santi, B. Revaz, J. Cortés *et al.*, "A Truly Redundant Aerial Manipulator System with Application to Push-and-Slide Inspection in Industrial Plants," *IEEE Robotics and Automation Letters*, vol. 4, no. 2, pp. 1846–1851, 2019.
- [4] S. Park, J. Lee, J. Ahn, M. Kim, J. Her, G.-H. Yang, and D. Lee, "ODAR: Aerial Manipulation Platform Enabling Omnidirectional Wrench Generation," *IEEE/ASME Transactions on Mechatronics*, vol. 23, no. 4, pp. 1907–1918, 2018.
- [5] M. Ryll, G. Muscio, F. Pierri, E. Cataldi, G. Antonelli, F. Caccavale, and A. Franchi, "6d physical interaction with a fully actuated aerial robot," in *2017 IEEE International Conference on Robotics and Automation (ICRA)*. IEEE, 2017, pp. 5190–5195.
- [6] ASCE, "2017 infrastructure report card." ASCE Reston, VA, 2017.
- [7] U. M. Angst, "Challenges and opportunities in corrosion of steel in concrete," *Materials and Structures*, vol. 51, no. 1, 2018.
- [8] B. Chan, H. Guan, J. Jo, and M. Blumenstein, "Towards UAV-based bridge inspection systems: A review and an application perspective," *Structural Monitoring and Maintenance*, vol. 2, no. 3, pp. 283–300, 2015.
- [9] P. Pfändler, K. Bodie, U. Angst, and R. Siegwart, "Flying corrosion inspection robot for corrosion monitoring of civil structures—first results," in *SMAR 2019—5th Conf. on Smart Monitoring, Assessment and Rehabilitation of Civil Structures*, 2019.
- [10] J. Isla and F. Cegla, "Emat phased array: A feasibility study of surface crack detection," *Ultrasonics*, vol. 78, pp. 1–9, 2017.
- [11] K. Bodie, Z. Taylor, M. Kamel, and R. Siegwart, "Towards Efficient Full Pose Omnidirectionality with Overactuated MAVs," in *International Symposium on Experimental Robotics (ISER)*. Springer, 2018.
- [12] F. Ruggiero, V. Lippiello, and A. Ollero, "Aerial manipulation: A literature review," *IEEE Robotics and Automation Letters*, vol. 3, no. 3, pp. 1957–1964, 2018.
- [13] A. Franchi, "Interaction control of platforms with multi-directional total thrust," in *Aerial Robotic Manipulation*. Springer, 2019, pp. 175–189.
- [14] H. Wopereis, L. van de Ridder, T. J. Lankhorst, L. Klooster, E. Bukai, D. Wuthier, G. Nikolakopoulos, S. Stramigioli, J. B. Engelen, and M. Fumagalli, "Multimodal Aerial Locomotion: An Approach to Active Tool Handling," *IEEE Robotics & Automation Magazine*, 2018.
- [15] M. Ryll, H. H. Bühlhoff, and P. R. Giordano, "A novel overactuated quadrotor unmanned aerial vehicle: Modeling, control, and experimental validation," *IEEE Transactions on Control Systems Technology*, vol. 23, no. 2, pp. 540–556, 2014.
- [16] F. Ruggiero, J. Cacace, H. Sadeghian, and V. Lippiello, "Passivity-based control of vtol uavs with a momentum-based estimator of external wrench and unmodeled dynamics," *Robotics and Autonomous Systems*, vol. 72, pp. 139–151, 2015.
- [17] T. Tomić, C. Ott, and S. Haddadin, "External Wrench Estimation, Collision Detection, and Reflex Reaction for Flying Robots," *IEEE Transactions on Robotics*, vol. 33, no. 6, pp. 1467–1482, 2017.
- [18] O. Khatib, "A unified approach for motion and force control of robot manipulators: The operational space formulation," *IEEE Journal on Robotics and Automation*, vol. 3, no. 1, pp. 43–53, 1987.
- [19] M. H. Raibert, J. J. Craig *et al.*, "Hybrid position/force control of manipulators," *Journal of Dynamic Systems, Measurement, and Control*, vol. 103, no. 2, pp. 126–133, 1981.
- [20] S. Haddadin, A. De Luca, and A. Albu-Schäffer, "Robot collisions: A survey on detection, isolation, and identification," *IEEE Transactions on Robotics*, vol. 33, no. 6, pp. 1292–1312, 2017.
- [21] C. Schindlbeck and S. Haddadin, "Unified passivity-based cartesian force/impedance control for rigid and flexible joint robots via task-energy tanks," in *2015 IEEE international conference on robotics and automation (ICRA)*. IEEE, 2015, pp. 440–447.
- [22] C. Richter, A. Bry, and N. Roy, "Polynomial trajectory planning for aggressive quadrotor flight in dense indoor environments," in *Robotics Research*. Springer, 2016, pp. 649–666.
- [23] K. Alexis, G. Darivianakis, M. Burri, and R. Siegwart, "Aerial robotic contact-based inspection: planning and control," *Autonomous Robots*, vol. 40, no. 4, pp. 631–655, 2016.
- [24] A. Bircher, K. Alexis, M. Burri, P. Oettershagen, S. Omari, T. Mantel, and R. Siegwart, "Structural inspection path planning via iterative viewpoint resampling with application to aerial robotics," in *2015 IEEE International Conference on Robotics and Automation (ICRA)*, May 2015, pp. 6423–6430.
- [25] K. Bodie, M. Brunner, M. Pantic, S. Walser, P. Pfändler, U. Angst, R. Siegwart, and J. Nieto, "An Omnidirectional Aerial Manipulation Platform for Contact-Based Inspection," in *Proceedings of Robotics: Science and Systems*, 2019.
- [26] F. Ruggiero, J. Cacace, H. Sadeghian, and V. Lippiello, "Impedance control of VTOL UAVs with a momentum-based external generalized forces estimator," in *2014 IEEE International Conference on Robotics and Automation (ICRA)*. IEEE, 2014, pp. 2093–2099.
- [27] N. Hogan, "Impedance control: An approach to manipulation: Part I: theory," 1985.
- [28] B. Siciliano, L. Sciacivico, L. Villani, and G. Oriolo, *Robotics: modelling, planning and control*. Springer Science & Business Media, 2010.
- [29] M. Kazhdan, M. Bolitho, and H. Hoppe, "Poisson surface reconstruction," in *Proceedings of the fourth Eurographics symposium on Geometry processing*, vol. 7, 2006.
- [30] L. Bertolini, B. Elsener, P. Pedferri, E. Redaelli, and R. B. Polder, *Corrosion of steel in concrete: prevention, diagnosis, repair*. John Wiley & Sons, 2013.

Karen Bodie is a PhD student at the Autonomous Systems Lab of ETH Zurich. Her research focuses on control and mechanical design of aerial robotic systems.

Maximilian Brunner is a PhD student at the Autonomous Systems Lab of ETH Zurich. He focuses on flight and interaction control of omni-directional MAVs.

Michael Pantic is a PhD student at the Autonomous Systems Lab of ETH Zurich. He works on perception and planning for omni-directional MAVs.

Stefan Walser is completing his master's degree in robotics, systems and control and is now working on his master thesis which focuses on system identification and control optimization using machine learning.

Patrick Pfändler is focused during his PhD in the corrosion assessment of reinforced concrete infrastructures by applying well-established non-destructive testing methods and by the on-site automation with robots.

Ueli Angst holds a SNSF professorship and leads the Durability of Engineering Materials Group at ETH Zurich, which is primarily concerned with corrosion of metals in various porous media and environments, such as steel in concrete or in soil.

Roland Siegwart is a full professor and leads the Autonomous Systems Lab at ETH Zurich. His research interests are in the design and control of systems operating in complex and highly dynamical environments

Juan Nieto is the deputy director of the Autonomous Systems Lab at ETH Zurich. His research focuses on perception and navigation for mobile robots.